remote sensing

MDPI

Article

Satellite Velocity Correction Method of Ocean Current Retrieval for a Spaceborne Doppler Scatterometer

Jingyu Zhang [1,2], Xiaolong Dong [1,2,3,*] and Di Zhu [1]

[1] CAS Key Laboratory of Microwave Remote Sensing, National Space Science Center, Chinese Academy of Sciences, Beijing 100190, China; zhangjingyu18@mails.ucas.ac.cn (J.Z.); zhudi@mirslab.cn (D.Z.)
[2] The School of Electronic, Electrical and Communication Engineering, University of Chinese Academy of Sciences, Beijing 100049, China
[3] The School of Astronomy and Space Science, University of Chinese Academy of Sciences, Beijing 100049, China
* Correspondence: dongxiaolong@mirslab.cn

Abstract: For a spaceborne pencil-beam rotating Doppler scatterometer, its precision in measuring the ocean surface motion depends on the Doppler centroid of the received signals. The Doppler centroid is determined by the relative motion between the scatterometer and the ocean surface. This relative motion includes contributions from satellite velocity, the phase velocity of resonant Bragg waves, the orbital motions of ocean waves, and the ocean surface current. Subtracting the contribution of the satellite platform velocity from the complex Doppler information is important for the application of a spaceborne Doppler scatterometer in ocean surface current retrieval. In this research, we propose a method for the platform velocity correction influenced by the Doppler centroid offset and analyze the accuracy of this correction method. The method is based on the echoed signal model of a Doppler scatterometer. Our results show that the offset could lead to a measurement offset of up to 0.02 m/s when the beam width was 0.3°. For a 0.6° beam width, the maximum offset was 0.07 m/s. Thus, with the high accuracy of the current spaceborne sensors' measurement, the offset can be accurately eliminated. In future applications and data processing algorithms, this effect should be considered.

Keywords: Doppler scatterometer; Doppler centroid; satellite velocity; ocean current

Citation: Zhang, J.; Dong, X.; Zhu, D. Satellite Velocity Correction Method of Ocean Current Retrieval for a Spaceborne Doppler Scatterometer. *Remote Sens.* **2023**, *15*, 5541. https://doi.org/10.3390/rs15235541

Academic Editor: Yukiharu Hisaki

Received: 26 October 2023
Revised: 18 November 2023
Accepted: 27 November 2023
Published: 28 November 2023

1. Introduction

Ocean surface currents play an important role in the air–sea exchanges of energy and heat [1,2], pollution dispersion (e.g., oil spills) [3], global climate balance, and other factors of scientific research and human activity security [4,5]. Given that the in-situ data are unavailable or incomplete in spatial scale in many parts of the world [6], using satellite data to directly measure the global ocean surface currents holds great importance and application value.

Currently, the spaceborne altimeter is the main instrument for obtaining global geostrophically derived ocean surface current information [7–9]. However, the ability of an altimeter to measure ocean surface currents is mainly limited to the quasi-geostrophic currents in off-equatorial open ocean areas. Moreover, it has the disadvantage of a long repeat observation period.

To overcome the disadvantages of spaceborne altimeters, researchers have proposed using Doppler shifts to directly observe ocean currents, such as retrieving ocean current information via spaceborne synthetic aperture radar (SAR) using the Doppler centroid anomaly method [10,11] and the along-track interferometry method [12,13]. Examples include ENVISAT's Advanced SAR instrument [14] and the proof experiment for the SEASTAR mission [15].

In recent years, Doppler scatterometers have drawn attention owing to their global coverage and two-component surface velocity measurement ability [16]. The Doppler

scatterometer is a new type of radar for ocean remote sensing that can measure the Doppler frequency shift. The ocean surface current parameters (two-component surface velocity) can be retrieved from the Doppler frequency shift of the received signal caused by the motion of the ocean surface [17].

Thus far, experiments based on airborne platforms and oceanographic platforms have been carried out globally on the mechanism of the Doppler scatterometer inversion method and the verification of the measurement principle. The NASA Jet Propulsion Laboratory developed a Ka-band pencil-beam Doppler scatterometer named DopplerScatt. They carried out an airborne experiment over the Mississippi River plume and Barataria Bay in 2017 and at the edge of a Gulf of Mexico Loop Current Eddy in 2018 [18,19]. Further, the Marine Hydrophysical Institute RAS carried out an experiment to measure Doppler frequency with a Ka-band Doppler scatterometer from an oceanographic platform in the Black Sea [20]. They developed a semi-empirical Doppler GMF (KaDOP) from the scatterometer data. The results confirm the ability of the Ka-band Doppler scatterometer to measure the ocean surface currents.

Previous theoretical analysis and experiments have shown that the pencil-beam scatterometer with the Ka-band achieves good performance. However, it remains difficult for us to obtain high-precision ocean surface current information from a spaceborne Doppler scatterometer. For a spaceborne pencil-beam rotating Doppler scatterometer, the pulse–pair method seems to be a reliable way to detect ocean surface motion [21]. However, its precision heavily depends on the correlation and the Doppler information of the received signals.

The measurement accuracy of ocean surface currents required by scientific research and other applications is 0.1 m/s [22]. To accurately obtain the ocean surface motion information from the scatterometer signals, we need to subtract the contribution of scatterometer platform velocity; that is, we need to propose a method to correct the influence of platform velocity.

Previous research has focused more on the surface current geophysical model function (GMF) and the contribution of effects, including long-wave modulation, Stokes orbit motion, and wind-driven ocean surface velocity, on the total Doppler frequency [18–20]. However, compared with a platform velocity of tens of meters per second under airborne conditions [23], a spaceborne Doppler scatterometer operates at a high velocity (several kilometers per second) [24]. This difference can lead to further complexity of signal processing or poor accuracy in the measurement of ocean surface velocity. Therefore, the correction of the platform velocity is important.

Currently, the precise orbit determinations (POD) mainly include Satellite Laser Ranging (SLR) [25], Doppler Orbitography and Radio-positioning Integrated by Satellite (DORIS) [26], Precise Range and Range Rate Equipment (PRARE) [27] and Global Navigation Satellite System (GNSS) [28,29]. The SLR system can obtain the distance with an accuracy of 0.5~5 cm. The DORIS system can obtain the distance with an accuracy of 0.5 mm/s. The PRARE data include the distance and velocity, with an accuracy of 2.5 cm and 0.25 mm/s, respectively. The GNSS system can obtain the satellite height with an orbit accuracy of 2 cm. Due to the high sampling rate, low cost, comprehensive coverage, and continuous observation, GNSS technology has been widely used in satellite orbit determination.

The Doppler frequency induced by satellite platform motion can be estimated using the satellite platform attitude and velocity information; however, it requires an accurate and precise measurement of the attitude and velocity information [11,17,18,30]. The effect of the satellite's attitude and velocity determinations on ocean current remote sensing has been analyzed in recent research.

Hansen et al. emphasized the need to accurately correct bias caused by geometrical Doppler shift prediction errors for ocean current retrieval using advanced synthetic aperture radar (ASAR) data in 2011 [11]. After bias correction, the root meansquare error of the

Doppler shift was 4.7 Hz for VV polarization, corresponding to a horizontal Doppler velocity of 0.23 m/s.

Bao et al. considered the error induced by satellite attitude determination and velocity errors as one of the sources of the ocean surface radial velocity error in their proposed ocean current retrieval method [31]. The ocean current velocity error induced by satellite attitude determination error could be as large as 0.25 m/s for a Ku-band scatterometer with an accuracy of 0.002° of satellite attitude determination.

Ardhuin et al. evaluated the error budget that satellite attitude error induced on the geometrical Doppler shift [24]. They pointed out that a specific algorithm is required to stabilize and decrease the platform attitude error for their Ka-band radar altimeter system. A strict satellite platform stability of 10^{-4} is necessary to ensure an acceptable radial velocity error.

Miao et al.'s results show that ocean current speed retrieval accuracy is sensitive to the accuracies of satellite attitude determination and velocity [32]. With an accuracy of 0.001° satellite attitude determination and 0.01 m/s for satellite speed accuracy, the total ocean current velocity retrieval error induced by satellite attitude determinations (including roll, pitch, and yaw) and velocity errors reached a maximum value of 0.16 m/s in the side-looking direction and a minimum value of 0.11 m/s in forward- and backward-looking directions. All these studies highlight the great importance of the accuracy of platform velocity elimination for ocean current retrieval.

In this research, we propose a method for platform velocity correction influenced by the Doppler centroid offset and analyze the accuracy of this correction method. The method is based on the echoed signal model of the Doppler scatterometer.

The rest of this paper is organized as follows. The ocean surface velocity measurement simulation process is introduced in Section 2. The velocity correction method of the influence of the Doppler centroid offset is presented in Section 3. The effects of satellite attitude and height determinations on the velocity correction are discussed in Section 4. Finally, the conclusions are provided in Section 5.

2. Materials and Methods

2.1. The Echoed Signal Simulation Model

The echoed signal simulation model was proposed in our previous work [33]. We assume that the spaceborne rotating pencil-beam Doppler scatterometer rotates clockwise. Let the scatterometer height be H; the scatterometer platform velocity is v_p; the radius of the Earth is R_E; the beam width of the antenna is β; and the incidence angle and azimuth angle are θ and φ, respectively. It is assumed that in the azimuth angle, 0° is the along-track direction, and 90°/270° is the cross-track direction. Figure 1 shows the observation geometry.

We can obtain the angle between the pencil-beam center and the near end of the beam by

$$\theta_N = \sin^{-1}\left[\frac{R_E+H}{R_E}\sin\left(\theta-\frac{\beta}{2}\right)\right]. \quad (1)$$

The distance from the near end of the beam to the scatterometer is given by

$$R_N = \left\{{R_E}^2 + (R_E+H)^2 - 2R_E(R_E+H)\cos\left[\theta_N - \left(\theta-\frac{\beta}{2}\right)\right]\right\}^{0.5}. \quad (2)$$

Similarly, the angle between the pencil-beam center and the far end of the beam is

$$\theta_F = \sin^{-1}\left[\frac{R_E+H}{R_E}\sin\left(\theta+\frac{\beta}{2}\right)\right]. \quad (3)$$

The distance from the far end of the beam to the scatterometer is given by

$$R_F = \left\{{R_E}^2 + (R_E+H)^2 - 2R_E(R_E+H)\cos\left[\theta_F - \left(\theta+\frac{\beta}{2}\right)\right]\right\}^{0.5}. \quad (4)$$

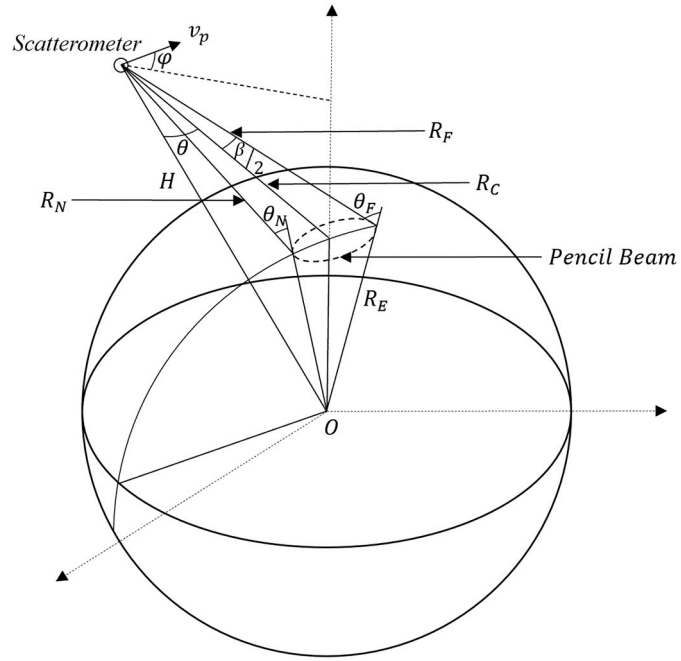

Figure 1. Observation geometry of the spaceborne Doppler scatterometer.

To simulate the echoed signal within the footprint, we divide the pencil beam footprint into grid nodes. Figure 2 shows the grid node division.

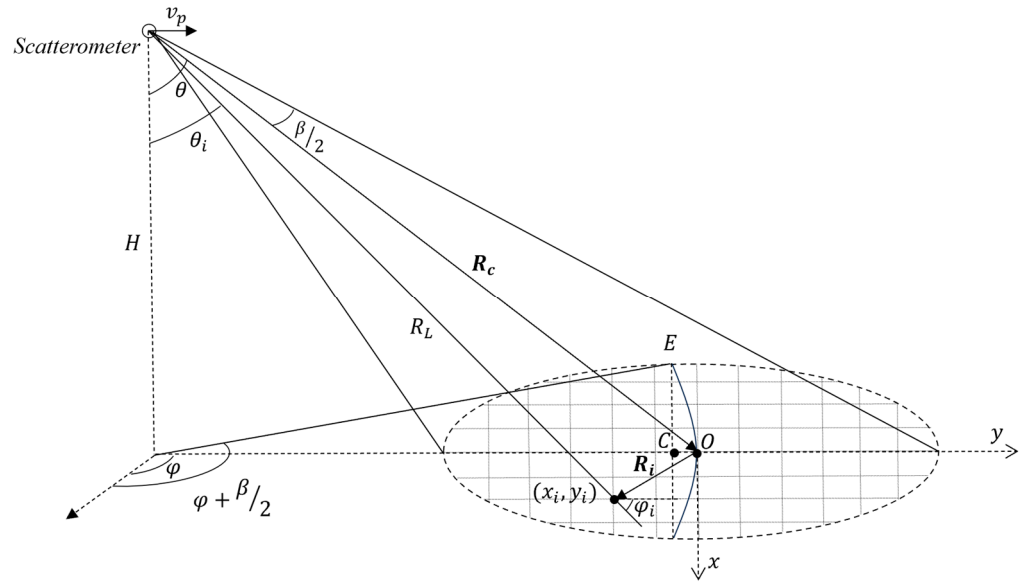

Figure 2. Grid node division of the footprint. Point O is the geometric center, point C is the actual Doppler centroid.

The pencil-beam footprint is divided into a 2D grid, where each grid node is at a different radial distance to the scatterometer and a different Doppler frequency. The distance from the ith grid node (x_i, y_i) to the scatterometer can be expressed as

$$R_L(i) = |\boldsymbol{R_c} + \boldsymbol{R_i}| \ , \tag{5}$$

Here, $\boldsymbol{R_c}$ is the radial vector from the scatterometer to the center of the footprint, and $\boldsymbol{R_i}$ represents the observation vector from the center of the footprint to the ith grid node.

The incidence angle of the ith grid node can be expressed as

$$\theta_i = \cos^{-1}\left[\frac{(R_E+H)^2+R_E^2-R_L(i)^2}{2R_E(R_E+H)}\right]. \quad (6)$$

The azimuth angle of the ith grid node can be expressed as

$$\varphi_i = \cos^{-1}\left\{\frac{H\tan\varphi\cos\theta-x_i}{\left[(-H\tan\varphi\cos\theta+x_i)^2+(H\tan\varphi\sin\theta+y_i)^2\right]^{0.5}}\right\}. \quad (7)$$

The Doppler frequency is given by [34]

$$f_D(i) = \frac{2v\cos\varphi_i\sin\theta_i}{\lambda}, \quad (8)$$

Here, v is the radial velocity between the grid node and the scatterometer.

The amplitude of the echoed signal is determined by the radar equation [35]:

$$A(i) = \left[\frac{P_t\lambda^2}{(4\pi)^3R_{Look}^4(i)}G(i)^2\frac{R_L(i)}{\sin\theta_i}\sigma_0(i)\right]^{0.5}, \quad (9)$$

Here, P_t is the transmitted power, and $G(i)$ is the antenna gain. We chose a Sinc antenna pattern for the simulation. $\sigma_0(i)$ is the backscattering coefficient related to the ocean surface roughness and slope.

Note that the influence of the modulation of backscatter coefficient in Equation (9) on the radial velocity measurement was analyzed in our previous work [33]. Therefore, we do not consider the influence of backscattering coefficient modulation in the analysis of the platform velocity correction in this research. The backscattering coefficient of each grid node is uniform. Under this assumption, the echoed signal amplitude becomes

$$A(i) = \left[\frac{P_t\lambda^2}{(4\pi)^3R_L^4(i)}G(i)^2\frac{R_L(i)}{\sin\theta_i}\right]^{0.5}. \quad (10)$$

The echoed signal is the superposition of each grid node weighted by the echoed signal power $A(i)$. We use a sinusoidal signal model to measure the Doppler frequency more accurately. Finally, the echoed signal is given by [36]

$$S = \sum S_i = \sum A_i\exp\{j2\pi[f_c + f_D(i) + f]t_i\}, \quad (11)$$

where f_c is the carrier frequency.

2.2. The Pulse–Pair Method

In Section 2.1, we simulated the received signal, so measuring the Doppler frequency (f_D) from the signal is the next step. For the rotating pencil-beam Doppler scatterometer, the pulse–pair method is used to obtain the radial velocity effectively via theoretical analysis and airborne validation experiments [21].

The principle of the pulse–pair method is to calculate the phase difference of two received signals to estimate the radial velocity. The pulse–pair method only involves signal processing in the time domain. Because of this simplicity, it is widely used for estimating Doppler frequency from backscattered signals in Doppler weather radar [37,38].

We assume that the two received signals are S_1 and S_2, the radial velocity between the scatterometer and the ocean surface is v, and the interval of the two signals is $\Delta\tau$. As shown in Figure 3, during time interval $\Delta\tau$, the relative position of the scatterometer and the ocean surface changes owing to the radial velocity (v). The change in the position leads to a phase difference of the two adjacent signals. By measuring the phase difference, we can obtain the radial velocity information.

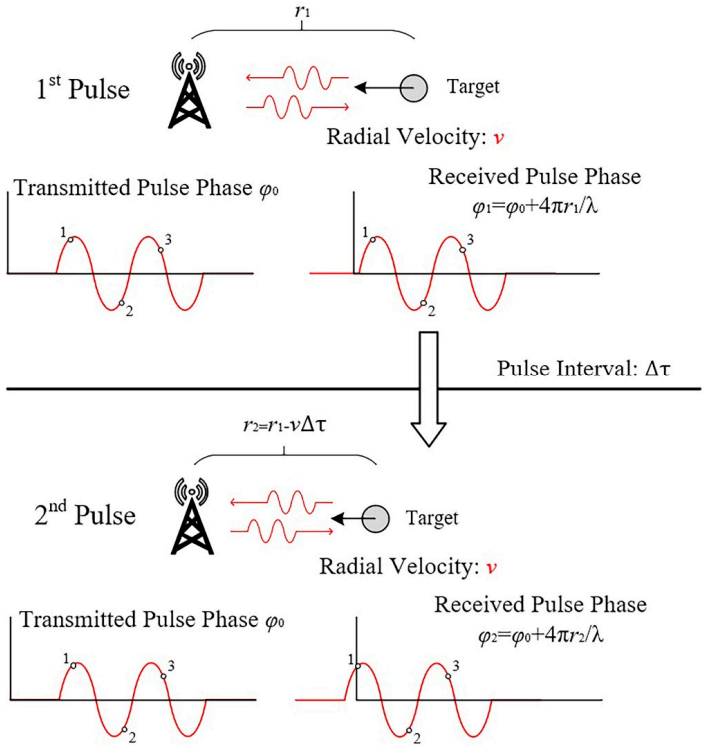

Figure 3. The principle of the pulse–pair method. Point 1–3 are three points at the same time in the two pulses to show the phase change between two pulses.

The change of distance can be expressed as

$$\Delta r = v\Delta\tau. \tag{12}$$

The Doppler frequency of radial velocity is

$$f = \frac{2v}{\lambda}. \tag{13}$$

The phase difference is given by

$$\Delta\varphi = 2\pi f\Delta\tau = \frac{4\pi v\Delta\tau}{\lambda}. \tag{14}$$

The two adjacent signals can be written as

$$S_1 = A_1\exp[j(2\pi ft + \varphi_0)], \tag{15}$$

$$S_2 = A_2\exp[j(2\pi ft + \Delta\varphi + \varphi_0)], \tag{16}$$

where A_1 and A_2 are the echoed signal amplitudes determined by Equation (10), and φ_0 is the initial phase.

The complex correlation coefficient of two signals (Γ) is given by

$$\begin{aligned}\Gamma &= S_1^* \cdot S_2 \\ &= A_1\exp[-j(2\pi ft + \varphi_0)] \cdot A_2\exp[j(2\pi ft + \Delta\varphi + \varphi_0)] \\ &= A_1A_2\exp(j\Delta\varphi).\end{aligned} \tag{17}$$

The interference phase (φ_{pp}) is the argument of the complex correlation coefficient, and it is given by

$$\varphi_{pp} = \tan^{-1}\left[\frac{Im(\Gamma)}{Re(\Gamma)}\right], \tag{18}$$

Here, φ_{pp} reflects the phase difference between pulses within the pencil beam of the Doppler scatterometer. If the relative motion is stable, a linear relationship exists between the phase difference and Doppler frequency. Therefore, the Doppler frequency (f_{pp}) obtained from the pulse–pair method can be expressed as

$$f_{pp} = \frac{1}{2\pi\tau}\tan^{-1}\left[\frac{Im(\Gamma)}{Re(\Gamma)}\right], \tag{19}$$

where τ is the interference interval. Then, the radial velocity can be obtained as follows:

$$v_{pp} = \frac{f_{pp}\lambda}{2}, \tag{20}$$

where λ is the wavelength.

2.3. Process of Measuring Ocean Surface Motion

The process of measuring ocean surface motion using the pulse–pair method was simulated with the model introduced in Sections 2.1 and 2.2 to evaluate the measurement error. The simulation process is shown in Figure 4.

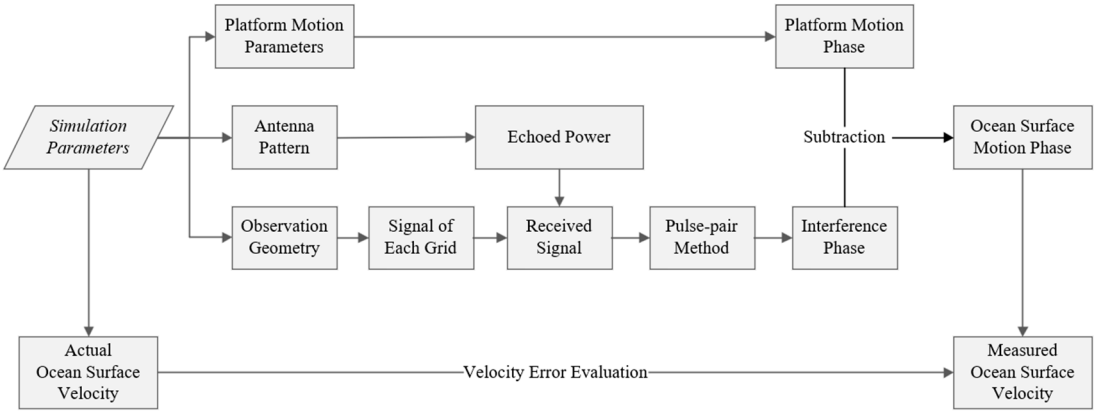

Figure 4. The process of measuring ocean surface motion.

We evaluated the pulse–pair method measurement errors under the spaceborne condition using the simulation model described above to analyze the effect of modulation and platform velocity. The parameters for this spaceborne condition were chosen to simulate the spaceborne Doppler scatterometer (DOPS) in the ocean surface current multi-scale observation mission (OSCOM) [22]. The key parameters are shown in Table 1.

Table 1. Key parameters of the simulation condition.

Parameters	Value
Platform Height (km)	520
Platform Velocity (m·s^{-1})	7000
Signal Frequency (GHz)	35.6
Beam Width (°)	0.3 (Ka)/0.6 (Ku)
Antenna Size (m)	1.5 (Ka)/0.8 (Ku)
Pulse Width (μs)	50
Pulse Repetition Time (μs)	100
Incidence Angle (°)	46

Using the echoed signal model and the pulse–pair method introduced in Sections 2.1 and 2.2, we could obtain the interference phase related to the platform motion and the ocean surface motion. First, we can calculate the theoretical ocean surface velocity v_{rS0} from the simulation parameters

$$v_{rS0} = \left(v_f + v_w + v_c\right)\sin\theta\cos\varphi. \tag{21}$$

where v_f is the wind-driven drift velocity [39]

$$v_f = 0.03\ U_{19.5}, \tag{22}$$

Here, $U_{19.5}$ is the wind speed at 19.5 m above the ocean surface.

v_w is the Stokes orbital velocity of the large-scale waves caused by the ocean surface gravitational waves [40].

$$v_w = \omega_p K_p \left(\frac{H_p}{2}\right)^2 \tag{23}$$

Here, K_p and H_p are the wavenumber and wave height of a fundamental wave. The fundamental wave corresponds to the wave at the spectral peak, related to the wind speed above the ocean surface. $\omega_p = 2\pi/T_p$ is related to the gravitational acceleration and wind speed, and v_c is the current velocity.

Then, we simulated the echoed signals by the model introduced in Section 2.1. The radial velocity v between the ocean surface and the scatterometer in Equation (8) is

$$v = v_{rS0} + v_p\sin\theta\cos\varphi, \tag{24}$$

where v_p is the platform velocity.

From two echoed signals, we can obtain the radial velocity using Equations (18)–(20) introduced in Section 2.2. To separate the ocean surface motion information from the measurement results, we subtracted the platform velocity contribution as follows [18]:

$$v_{rS} = \frac{1}{\sin\theta}\left(\frac{\varphi_{pp}\lambda}{4\pi\tau} - v_p\sin\theta\cos\varphi\right), \tag{25}$$

Here, θ is the incidence angle; φ is the azimuth angle; φ_{pp} is the interference phase; τ is the interference interval.

Parameter v_{rS} eliminates the contribution of platform velocity. It includes several effects, such as long-wave modulation, Stokes orbit motion, and wind-driven ocean surface velocity. In our evaluation of the radial velocity error, we primarily focused on the Doppler frequency related to the total ocean surface velocity (v_{rS}), which encompasses the combined effects of wind and waves. By comparing the measured radial velocity v_{rS} compared with the theoretical velocity v_{rS0}, we can evaluate the measurement offset.

We attempted to eliminate the effect of platform velocity using Equation (25) and found that this could result in a significant measurement error in the spaceborne scenario owing to the offset of Doppler centroid. Under the conditions of a spaceborne platform, an offset was observed between the radial velocity measured by the pulse–pair method and the real ocean surface velocity.

Figure 5a shows the measured radial velocity with beam widths of 0.3° and 0.6° and the theoretical velocity. Figure 5b shows the radial velocity offset with beam widths of 0.3° and 0.6°. The maximum offset was 0.02 m/s when the beam width was 0.3°. For the 0.6° beam width, the maximum offset was 0.07 m/s.

In the next section, we analyze the sources of the offset and propose a method for platform velocity correction.

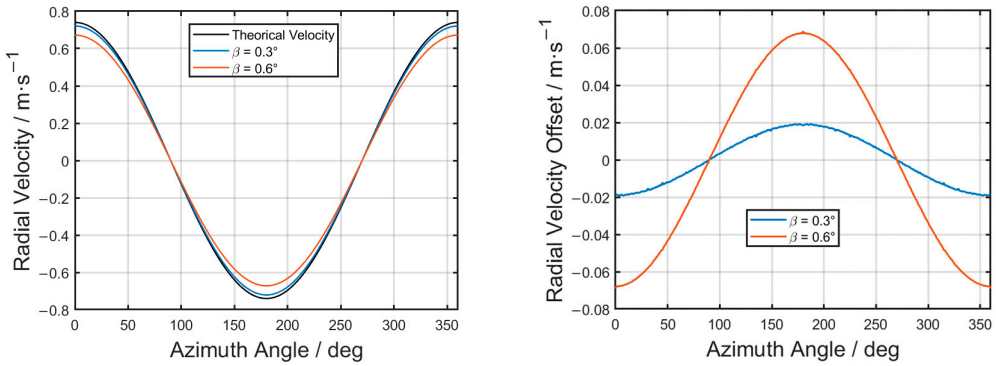

Figure 5. (**a**) The measured radial velocity v_{rS} compared with the theoretical velocity v_{rS0}. (**b**) Radial velocity offset.

3. The Velocity Correction Method

3.1. Analysis of the Doppler Spectrum

To analyze the velocity offset, we analyzed the Doppler spectrum within the beam width in the along-track direction. From the received signal, we could obtain the Doppler spectrum from the Fourier transform of the received signal (S) with Equation (11). First, the carrier frequency was removed as follows:

$$S_D = S \cdot e^{-j2\pi f_c t} = \sum A_i \exp\{j2\pi[f_D(i) + f]t_i\}. \tag{26}$$

The Doppler spectrum (F'_D) is the Fourier transform of the signal S_D

$$F'_D(f) = \int_{-\infty}^{+\infty} S_D e^{-j2\pi ft} dt. \tag{27}$$

Before the analysis of the Doppler spectrum, the platform velocity contribution is subtracted as follows:

$$F_D(f) = F'_D(f) - v_p \sin\theta \cos\varphi. \tag{28}$$

For simplicity, we first considered that the echoed power of the signal is not modulated by the antenna pattern.

Figure 6 shows the Doppler spectrum of the received signal in the footprint. The theoretical Doppler centroid f_{rS0} in Figure 6 is calculated from the theoretical velocity v_{rS0} in Equation (21):

$$f_{rS0} = \frac{2v_{rS0}}{\lambda}. \tag{29}$$

For a middle wind speed (10 m/s), when the current velocity is set to 0.1m/s, the theoretical Doppler centroid f_{rS0} is about 194 Hz. The Doppler spectrum was not symmetrical about the theoretical Doppler centroid but had a certain skewness. The asymmetry made the Doppler spectrum centroid of the footprint (solid line) and the theoretical Doppler centroid (dashed line) unequal. Therefore, when we used the theoretical Doppler centroid of the beam for platform motion correction in the process of measuring ocean surface motion (Section 2.3), the measured ocean surface velocity would be offset.

Figure 7 shows the equidistant line of the footprint. Because the footprint had a certain width, the equidistant line of the panel in the azimuth direction was not perpendicular to the observation direction, which led to the Doppler centroid in the footprint being closer to the scatterometer than the geometric center of the beam.

The geometric center of the beam could not be equivalent to the Doppler center of the beam. Therefore, we used the actual Doppler centroid instead of the geometric center to correct the platform velocity. This Doppler centroid offset was not handled in the process of measuring ocean surface motion introduced in Section 2.3. For the

combined Doppler frequency obtained by the pulse–pair method, the platform Doppler frequency corresponding to the geometric center of the beam was simply subtracted, so the measurement result had an offset value that could not be ignored.

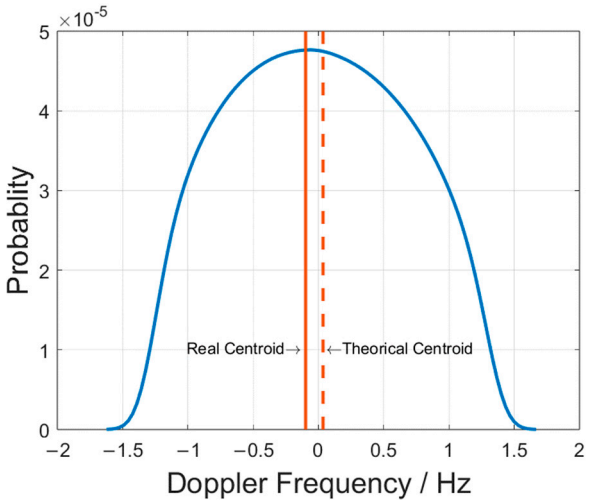

Figure 6. Doppler spectrum of the received signal in the footprint.

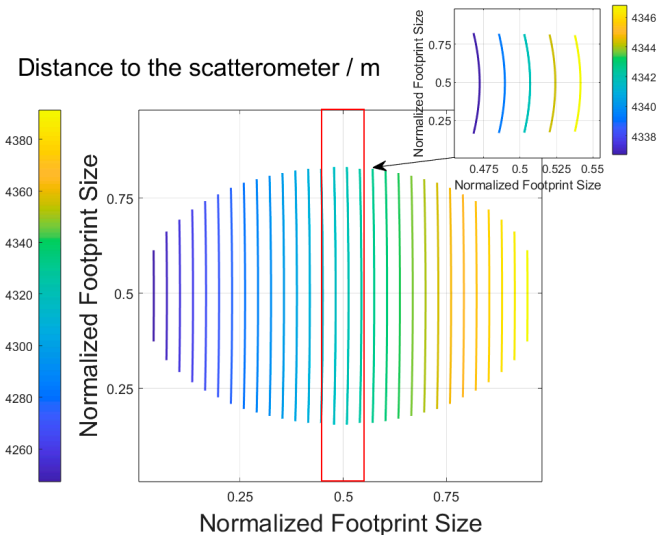

Figure 7. Equidistant line of the footprint.

The above analysis of Doppler centroid offset did not factor in the antenna pattern modulation. When we considered the antenna pattern modulation effect, the energy of the Doppler frequency at the beam geometric center was the highest, and the energy gradually decreased with the increase in the distance between the grid node and the beam geometric center.

Figure 8 shows the offset considering and not considering the antenna pattern modulation. If the antenna pattern was the Sinc pattern, the antenna pattern modulation would reduce the energy of the actual Doppler centroid, resulting in the further offset of the measurement results. The offset reached a maximum of ± 0.018 m/s in the along-track direction without antenna pattern modulation; when we factored in the antenna pattern modulation, the offset increased further, and the maximum was about ± 0.025 m/s in the along-track direction.

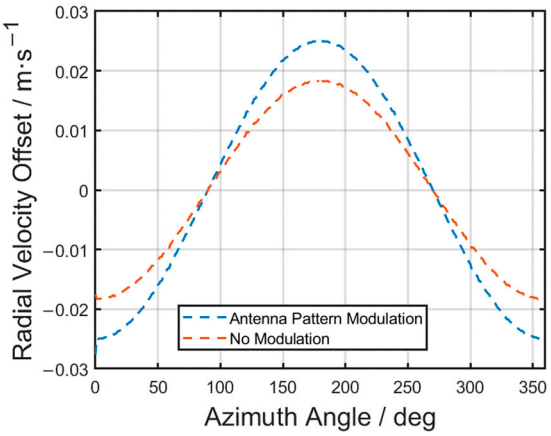

Figure 8. The offset considering and not considering the antenna pattern modulation.

For the ocean surface current measurement, the requirement of overall measurement accuracy was 0.1 m/s. The offset accounted for 25% of the accuracy requirement. Therefore, we had to conduct further analyses of this offset and propose a method for correcting the platform velocity accurately.

3.2. Offset between Doppler Centroid and Geometric Center within Footprint

As shown in Figure 2, the actual Doppler centroid of the beam (point *C*) was the centroid of the Doppler frequency on the equidistant line where the geometric center point *O* of the beam center was located. The distance between the actual center of the beam and the platform R_{rC} is given by

$$R_{rC} = \frac{H}{\cos\theta}\cos\left(\frac{\beta}{2}\right). \tag{30}$$

Then, the incidence angle (θ_C) and azimuth angle (φ_C) of the actual centroid *C* are given by

$$\theta_C = \cos^{-1}\left(\frac{\cos\theta}{\cos\left(\frac{\beta}{2}\right)}\right), \tag{31}$$

$$\varphi_C = \varphi. \tag{32}$$

The offset of radial velocity can be expressed as

$$\begin{aligned} v_o(\theta, \varphi, v_P) &= v_P(cos\varphi sin\theta - cos\varphi_C sin\theta_C) \\ &= v_P cos\varphi\left(sin\theta - \frac{\sqrt{cos^2\left(\frac{\beta}{2}\right) - cos^2\theta}}{cos\left(\frac{\beta}{2}\right)}\right). \end{aligned} \tag{33}$$

Figure 9 shows that the offset in the cross-track direction was 0, while the offset in the along-track direction was the largest. With the increase in incidence angle, the offset decreased from 0.036/s at a 30° incidence angle to 0.007 m/s at a 60° incidence angle.

Using the satellite platform velocity and the observed geometric parameters, we subtracted the platform velocity under the influence of the Doppler centroid offset. The velocity correction $v_c(\theta, \varphi, v_P)$ was the reverse of the offset $v_o(\theta, \varphi, v_P)$:

$$v_c(\theta, \varphi, v_P) = -v_o(\theta, \varphi, v_P). \tag{34}$$

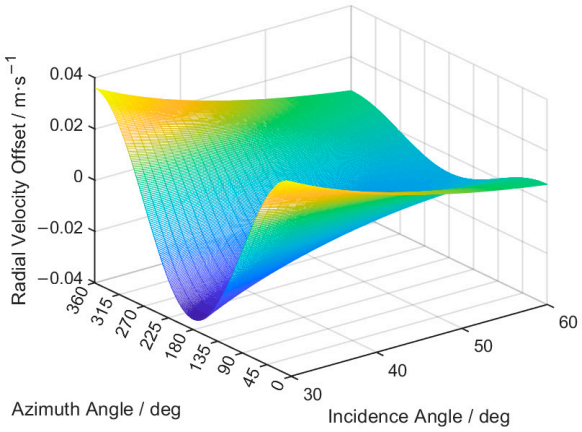

Figure 9. Radial velocity offset (v_o) with azimuth angle and incidence angle.

In this case, the subtraction of platform velocity (Equation (25)) becomes

$$v_{rS} = \frac{1}{\sin\theta}\left(\frac{\varphi_{pp}\lambda}{4\pi\tau} - \boldsymbol{l}\cdot\boldsymbol{v_p} - v_c(\theta,\varphi,v_P)\right). \tag{35}$$

3.3. Offset Considering Antenna Pattern

Assume that the antenna adopts a Sinc pattern [41], the following holds:

$$G(\theta,\varphi) = G_0\left[\frac{\sin(2.773\theta/\beta_\theta)}{2.773\theta/\beta_\theta}\right]^2\left[\frac{\sin(2.773\varphi/\beta_\varphi)}{2.773\varphi/\beta_\varphi}\right]^2, \tag{36}$$

where G_0 is the antenna gain; θ is the incidence angle; φ is the azimuth angle; and β_θ and β_φ are the beam width in the incidence and azimuth directions, respectively.

Figure 10 shows the antenna pattern. At the edge of the beam, the amplitude was half of the maximum.

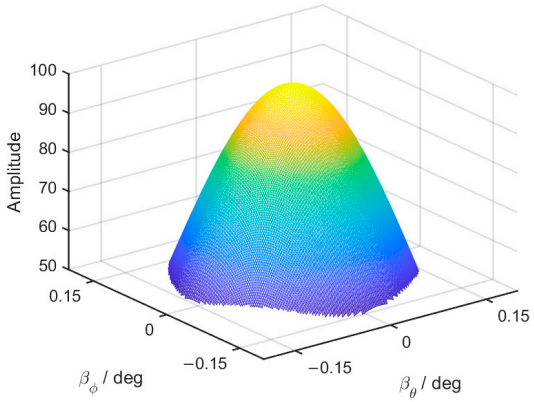

Figure 10. Antenna pattern with an antenna gain of 20 dB and a beam width of 0.3° in both the elevation and azimuth directions.

The incidence angle (θ_C) and azimuth angle (φ_C) of the actual Doppler centroid are given by Equations (31) and (32). So, the antenna gain of the Doppler centroid is given by

$$G_C = G(\theta_C,\varphi_C). \tag{37}$$

and the correction of the platform velocity is given by

$$v_{cG}(\theta,\varphi,v_P) = -v_{oG}(\theta,\varphi,v_P) = -\frac{G_C}{G_0}v_o(\theta,\varphi,v_P). \tag{38}$$

Using Equation (38), we can calculate the offset of the Doppler centroid, considering the influence of antenna pattern modulation. Figure 11 shows the offset of the radial velocity with a beam width of 0.3° at different incidence angles and azimuth angles. The offset reached the maximum in the along-track direction. With the increase in incidence angle, the offset decreased gradually, from the maximum, 0.01 m/s at a 30° incidence angle, to the minimum, 0.004 m/s at a 60° incidence angle. Compared with the offset without antenna pattern modulation, the offset with antenna pattern modulation increased by about 65%.

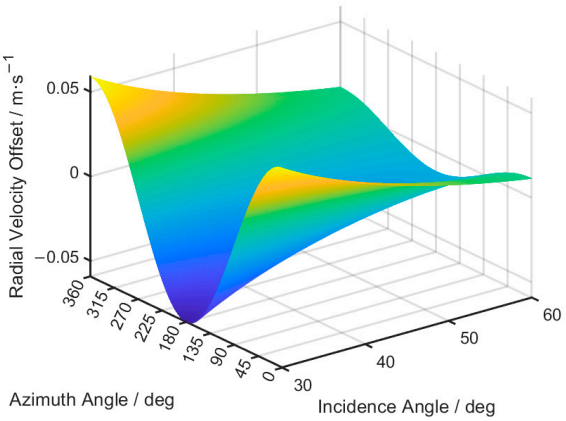

Figure 11. Offset of the Doppler centroid, considering the influence of antenna pattern modulation with incidence angle and azimuth angle.

4. Discussion

In Section 3, we established the correction method of platform velocity. From Equations (33) and (34), it can be seen that the incidence angle, azimuth angle, and satellite platform velocity affect the correction accuracy. Next, we further analyze the correction accuracy.

According to the total differential equation, the correction error can be deconstructed into the errors of the above-mentioned factors, as follows:

$$\Delta v_c(\theta, \varphi, v_P) = \frac{\partial v_c(\theta, \varphi, v_P)}{\partial \theta} \cdot \Delta\theta + \frac{\partial v_c(\theta, \varphi, v_P)}{\partial \varphi} \cdot \Delta\varphi + \frac{\partial v_c(\theta, \varphi, v_P)}{\partial v_P} \cdot \Delta v_P, \tag{39}$$

where $\Delta\theta$ is the measurement error of incidence angle, $\Delta\varphi$ is the measurement error of azimuth angle, and Δv_P is the measurement error of satellite platform velocity. Next, we analyze the error caused by each determination.

4.1. The Derivative of Determinations

4.1.1. The Derivative of the Correction Velocity to the Incidence Angle

From Equations (34) and (39), we can obtain the following derivatives:

$$\begin{aligned} \frac{\partial v_c(\theta,\varphi,v_P)}{\partial \theta} &= \frac{\partial}{\partial \theta}\left[-v_P \cos\varphi \left(\sin\theta - \frac{\sqrt{\cos^2\left(\frac{\beta}{2}\right) - \cos^2\theta}}{\cos\left(\frac{\beta}{2}\right)}\right)\right] \\ &= -v_P \cos\varphi \left(\cos\theta - \left(\frac{\cos\theta\sin\theta}{\cos\left(\frac{\beta}{2}\right)\sqrt{\cos^2\left(\frac{\beta}{2}\right) - \cos^2\theta}}\right)\right) \end{aligned} \tag{40}$$

As shown in Figure 12, the effect of incidence angle determination on the platform velocity correction reached the maximum in the along-track direction (0°). With the increase in the incidence angle, the effect decreased.

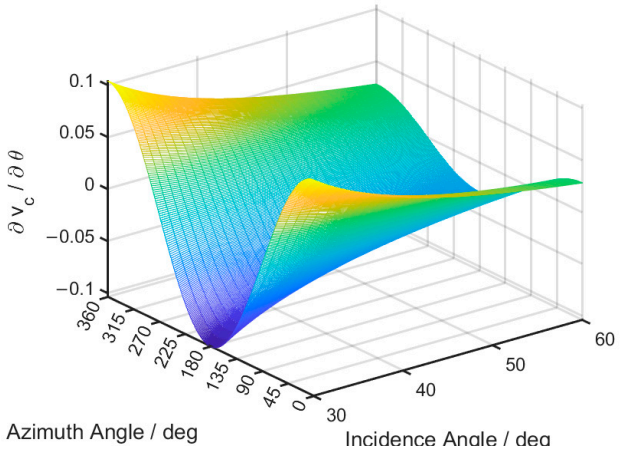

Figure 12. Derivative of the correction velocity to the incidence angle.

4.1.2. The Derivative of the Correction Velocity to the Azimuth Angle

The derivative of the correction velocity to the azimuth angle is calculated using Equation (41). Figure 13 shows that, contrary to the incidence angle determination, the azimuth angle determination had the greatest impact on the platform velocity correction in the cross-track direction (90° and 270°). With the increase in the incidence angle, the effect decreased.

$$\begin{aligned} \frac{\partial v_c(\theta,\varphi,v_P)}{\partial \varphi} &= \frac{\partial}{\partial \varphi}\left[-v_P \cos\varphi\left(\sin\theta - \frac{\sqrt{\cos^2\left(\frac{\beta}{2}\right)-\cos^2\theta}}{\cos\left(\frac{\beta}{2}\right)}\right)\right] \\ &= v_P sin\varphi\left(\sin\theta - \frac{\sqrt{\cos^2\left(\frac{\beta}{2}\right)-\cos^2\theta}}{\cos\left(\frac{\beta}{2}\right)}\right) \end{aligned} \tag{41}$$

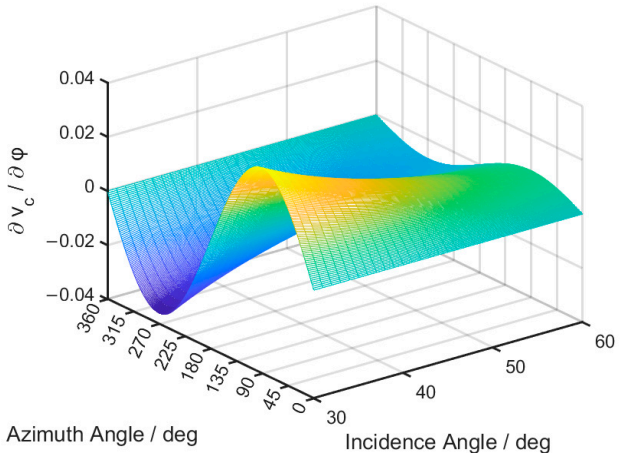

Figure 13. Derivative of the correction velocity to the azimuth angle.

4.1.3. The Derivative of the Correction Velocity to the Platform Velocity

The derivative of the correction velocity to the platform velocity is calculated with Equation (42). Figure 14 shows that the effect of platform velocity determination on the

platform velocity correction reached its maximum in the along-track direction (0° and 180°). With the increase in incidence angle, the effect decreased gradually.

$$\begin{aligned}\frac{\partial v_c(\theta,\varphi,v_P)}{\partial v_P} &= \frac{\partial}{\partial v_P}\left[-v_P\cos\varphi\left(\sin\theta-\frac{\sqrt{\cos^2\left(\frac{\beta}{2}\right)-\cos^2\theta}}{\cos\left(\frac{\beta}{2}\right)}\right)\right]\\ &= -\cos\varphi\left(\sin\theta-\frac{\sqrt{\cos^2\left(\frac{\beta}{2}\right)-\cos^2\theta}}{\cos\left(\frac{\beta}{2}\right)}\right).\end{aligned} \tag{42}$$

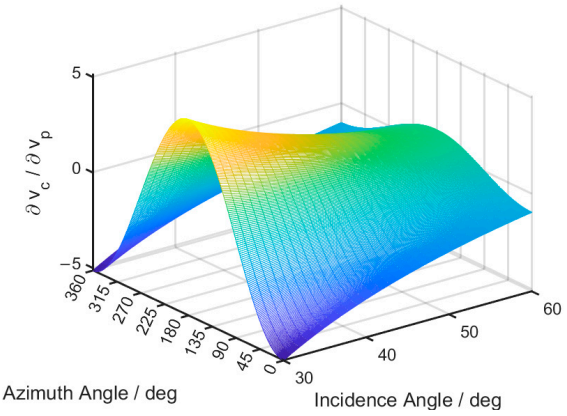

Figure 14. Derivative of the correction velocity to the platform velocity.

Moreover, comparing the size of each component, we found that the maximum values of $\frac{\partial v_c(\theta,\varphi,v_P)}{\partial\theta}$ and $\frac{\partial v_c(\theta,\varphi,v_P)}{\partial\varphi}$ were similar and that the maximum value of $\frac{\partial v_c(\theta,\varphi,v_P)}{\partial v_P}$ was four orders of magnitude smaller than the former two.

4.2. Contribution of the Satellite Attitude

The measurement errors of the incidence angle and azimuth angle are caused by satellite attitude determinations. The satellite attitude contains the pitch, yaw, and roll. Thus, we had to convert the satellite attitude (i.e., yaw, pitch, and roll) into the incidence angle and azimuth angle. The transformation matrix can be written as follows [42]:

$$\begin{aligned}\boldsymbol{T_p} &= \boldsymbol{T_p^y}\cdot\boldsymbol{T_p^p}\cdot\boldsymbol{T_p^r}\\ &= \begin{bmatrix}\cos\psi_y & -\sin\psi_y & 0\\ \sin\psi_y & \cos\psi_y & 0\\ 0 & 0 & 1\end{bmatrix}\begin{bmatrix}\cos\psi_p & 0 & \sin\psi_p\\ 0 & 1 & 0\\ -\sin\psi_p & 0 & \cos\psi_p\end{bmatrix}\begin{bmatrix}1 & 0 & 0\\ 0 & \cos\psi_r & -\sin\psi_r\\ 0 & \sin\psi_r & \cos\psi_r\end{bmatrix}\\ &= \begin{bmatrix}\cos\psi_y\cos\psi_p-\sin\psi_y\sin\psi_p\sin\psi_r & -\sin\psi_y\cos\psi_r & \cos\psi_y\sin\psi_p+\sin\psi_y\cos\psi_p\sin\psi_r\\ \sin\psi_y\cos\psi_p+\cos\psi_y\sin\psi_p\sin\psi_r & \cos\psi_y\cos\psi_r & \sin\psi_y\sin\psi_p-cos\psi_y\cos\psi_p\sin\psi_r\\ -\cos\psi_y\sin\psi_p & \sin\psi_r & \cos\psi_y\cos\psi_p\end{bmatrix}\end{aligned} \tag{43}$$

According to the transformation matrix, we could transfer the yaw/pitch/roll parameters to the incidence/azimuth parameters; thus, we could analyze the error of the radial velocity correction.

4.2.1. Yaw

With a yaw angle of ψ_y, the radial direction vector $\vec{R_l^y}$ can be written as follows:

$$\begin{aligned}\vec{R_l^y} &= \boldsymbol{T_p^y}\cdot\vec{R_l}\\ &= \begin{bmatrix}\cos\psi_y & -\sin\psi_y & 0\\ \sin\psi_y & \cos\psi_y & 0\\ 0 & 0 & 1\end{bmatrix}\begin{bmatrix}\sin\theta cos\varphi\\ \sin\theta\sin\varphi\\ -cos\theta\end{bmatrix} = \begin{bmatrix}\sin\theta cos(\varphi+\psi_y)\\ \sin\theta\sin(\varphi+\psi_y)\\ -cos\theta\end{bmatrix}\end{aligned} \tag{44}$$

Then, the incidence angle θ_y is the angle between the radial vector $\vec{R_l^y}$ and the radial vector from the scatterometer to the nadir point $\vec{R_n} = (0, 0, -1)$, and is given by

$$\theta_y = \cos^{-1}\left(\vec{R_l^y} \cdot \vec{R_n}\right) = \theta. \tag{45}$$

The azimuth angle φ_y can be expressed as follows:

$$\varphi_y = \tan^{-1}\left(\frac{\sin\theta\sin(\varphi + \psi_y)}{\sin\theta\cos(\varphi + \psi_y)}\right) = \varphi + \psi_y. \tag{46}$$

The error caused by ψ_y is given by

$$\Delta\theta_y = \theta_y - \theta,\ \Delta\varphi_y = \varphi_y - \varphi. \tag{47}$$

4.2.2. Pitch

Like the yaw, with a pitch angle of ψ_p, the radial direction vector is given by

$$\begin{aligned}\vec{R_l^p} &= \boldsymbol{T_p^y} \cdot \vec{R_l} \\ &= \begin{bmatrix} \cos\psi_p & 0 & \sin\psi_p \\ 0 & 1 & 0 \\ -\sin\psi_p & 0 & \cos\psi_p \end{bmatrix} \begin{bmatrix} \sin\theta cos\varphi \\ \sin\theta\sin\varphi \\ -cos\theta \end{bmatrix} = \begin{bmatrix} \sin\theta cos\varphi\cos\psi_p - cos\theta\sin\psi_p \\ \sin\theta\sin\varphi \\ -\sin\theta cos\varphi\sin\psi_p - cos\theta cos\psi_p \end{bmatrix}.\end{aligned} \tag{48}$$

The incidence angle θ_p is given by

$$\theta_p = \cos^{-1}\left(\vec{R_l^y} \cdot \vec{R_n}\right) = \cos^{-1}\left(\sin\theta cos\varphi\sin\psi_p + cos\theta cos\psi_p\right). \tag{49}$$

The azimuth angle φ_p can be expressed as follows:

$$\varphi_p = \tan^{-1}\left(\frac{\sin\theta\sin\varphi}{\sin\theta cos\varphi\cos\psi_p - cos\theta\sin\psi_p}\right). \tag{50}$$

The error caused by ψ_p is given by

$$\Delta\theta_p = \theta_p - \theta,\ \Delta\varphi_p = \varphi_p - \varphi. \tag{51}$$

4.2.3. Roll

Similarly, with a roll angle of ψ_r, the radial direction vector can be expressed as follows:

$$\begin{aligned}\vec{R_l^r} &= \boldsymbol{T_p^r} \cdot \vec{R_l} \\ &= \begin{bmatrix} 1 & 0 & 0 \\ 0 & \cos\psi_r & -\sin\psi_r \\ 0 & \sin\psi_r & \cos\psi_r \end{bmatrix} \begin{bmatrix} \sin\theta cos\varphi \\ \sin\theta\sin\varphi \\ -cos\theta \end{bmatrix} = \begin{bmatrix} \sin\theta cos\varphi \\ \sin\theta\sin\varphi cos\psi_r + cos\theta\sin\psi_r \\ \sin\theta\sin\varphi\sin\psi_r - cos\theta cos\psi_r \end{bmatrix}.\end{aligned} \tag{52}$$

The incidence angle θ_r is given by

$$\theta_r = \cos^{-1}\left(\vec{R_l^r} \cdot \vec{R_n}\right) = \cos^{-1}(-\sin\theta\sin\varphi\sin\psi_r + cos\theta cos\psi_r). \tag{53}$$

The azimuth angle φ_r can be expressed as follows:

$$\varphi_r = \tan^{-1}\left(\frac{\sin\theta cos\varphi cos\psi_r + cos\theta\sin\psi_r}{\sin\theta cos\varphi}\right). \tag{54}$$

The error caused by ψ_r is given by

$$\Delta\theta_r = \theta_r - \theta,\ \Delta\varphi_r = \varphi_r - \varphi. \tag{55}$$

The variations in incidence angle and azimuth angle errors caused by the yaw, the pitch, and the roll with the azimuth angle are shown in Figure 15. For the scatterometer attitude determinations, a determination of 0.0005° is reasonable for high-accuracy star sensors [43]. Therefore, we set the yaw, pitch, and roll determinations to 0.0005° in the simulation.

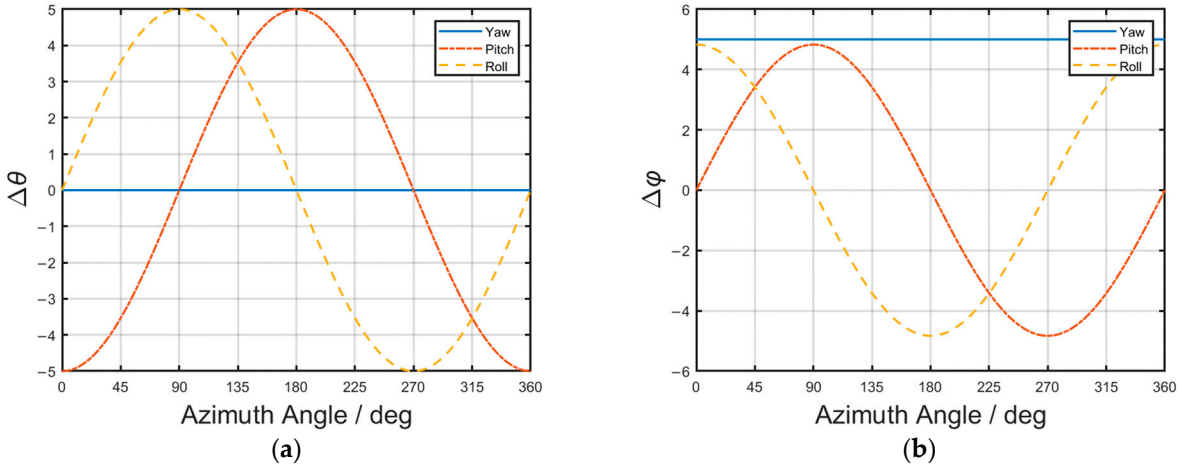

Figure 15. Effects of the scatterometer attitude determinations on (**a**) incidence angle error and (**b**) azimuth angle error.

As shown in Figure 15a, for the incidence angle error, the yaw determination had no effect, while the effect of roll determination on the incidence angle reached the peak in the cross-track direction (90° and 270°), and the pitch determination's effect on the incidence angle reached the peak in the along-track direction (0° and 180°). For the azimuth angle error in Figure 15b, the yaw determination effect was constant; it did not change with the azimuth angle. The roll determination effect on the azimuth angle was the largest in the along-track direction, and the pitch determination effect on the azimuth angle was the largest in the cross-track direction.

With the transformation of the determinations, we can calculate the effects of satellite attitude determinations on the correction error from Equation (39).

Figure 16 shows the effects of each satellite attitude determination on the error of correction. The effect of yaw determination on the error of correction reached the peak in the cross-track direction, and the effect of pitch determination reached the maximum in the along-track direction. The effect of roll determination reached the maximum in the 45° and 135° directions, and its effect became 0 in the along-track and cross-track directions. The effects of satellite attitude determinations were at a consistent order of magnitude.

4.3. Contribution of the Platform Velocity

The measurement errors in the satellite platform velocity were caused by the satellite orbit altitude determination. To analyze the contribution of platform velocity to the measurement error, assuming that the satellite orbit is circular, we can describe the relationship between platform height (H) and platform velocity (v_p) as follows:

$$v_p = \sqrt{\frac{GM}{H + R_E}}. \tag{56}$$

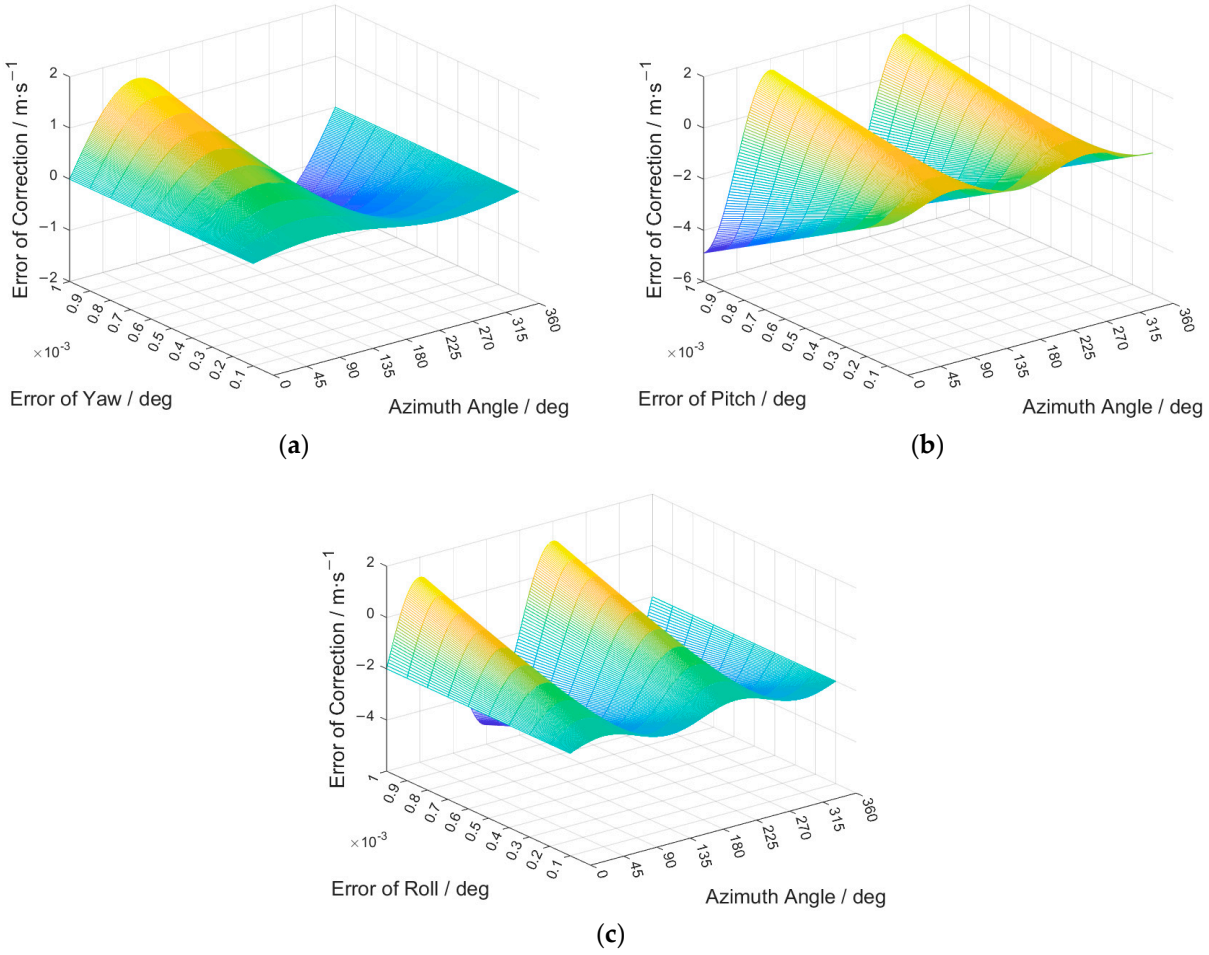

Figure 16. Effects of each satellite attitude determination on the error of correction. (**a**) Yaw. (**b**) Pitch. (**c**) Roll.

The error of platform velocity can be expressed as follows:

$$\Delta v_p = \frac{d\sqrt{\frac{GM}{H+R_E}}}{\mathrm{d}H}\Delta H = \frac{-\sqrt{GM}}{2(H+R_E)^{1.5}}\Delta H. \tag{57}$$

As shown in Figure 17, similar to the satellite attitude determinations, the effect of platform velocity determination was on $\frac{\partial v_c(\theta,\varphi,v_P)}{\partial v_P}\cdot\Delta v_P$ only. Thus, the correction error Equation (39) could be written as follows:

$$\Delta v_{cH} = -\cos\varphi\left(\sin\theta - \frac{\sqrt{\cos^2\left(\frac{\beta}{2}\right)-\cos^2\theta}}{\cos\left(\frac{\beta}{2}\right)}\right)\cdot\Delta v_P. \tag{58}$$

As shown in Figure 18, the correction error increased with the satellite platform height error. In the cross-track direction, the effect of platform height determination on correction error reached the maximum. High-precision satellite height measurement sensors could reduce the error to 10 m [44], so the maximum was less than $2\times10^{-8}\mathrm{m\cdot s^{-1}}$. This is much smaller than the correction.

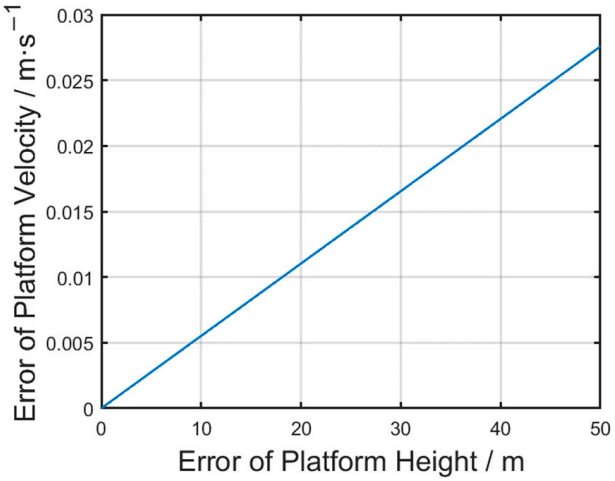

Figure 17. Error of satellite platform velocity with error of platform height.

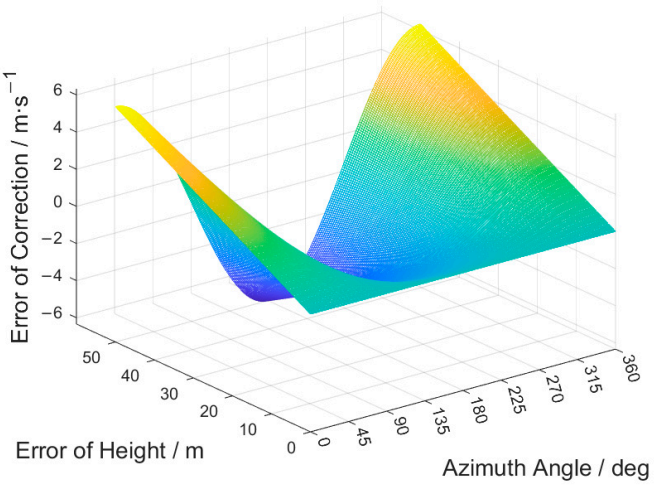

Figure 18. Effect of satellite height determination on the correction error.

4.4. Total Effects of Satellite Attitude and Height Determinations on the Correction

The yaw, pitch, roll, and platform height determinations are random and mutually independent variables, so the correction errors caused by scatterometer attitude and height determinations could be expressed as follows:

$$\Delta v_c(\theta, \varphi, v_P) = \sqrt{\Delta {v_{cy}}^2 + \Delta {v_{cp}}^2 + \Delta {v_{cr}}^2 + \Delta {v_{cH}}^2}, \tag{59}$$

where Δv_{cy}, Δv_{cp}, Δv_{cr}, and Δv_{cH} denote yaw, pitch, roll, and satellite platform height determination, respectively.

The total effects of determinations above with beam widths of 0.3° and 0.6° are shown in Figure 19. Figure 19a shows that with a beam width of 0.3°, using current high-precision satellite attitude and altitude measurement technology, the overall error of velocity correction could be reduced to 5×10^{-5} m/s. Figure 19b shows that for a beam width of 0.6°, the overall error of velocity correction could be reduced to 2×10^{-4} m/s.

The sensitivity of velocity determination to each determination and the error contribution of each determination under a 46° incidence angle are shown in Table 2.

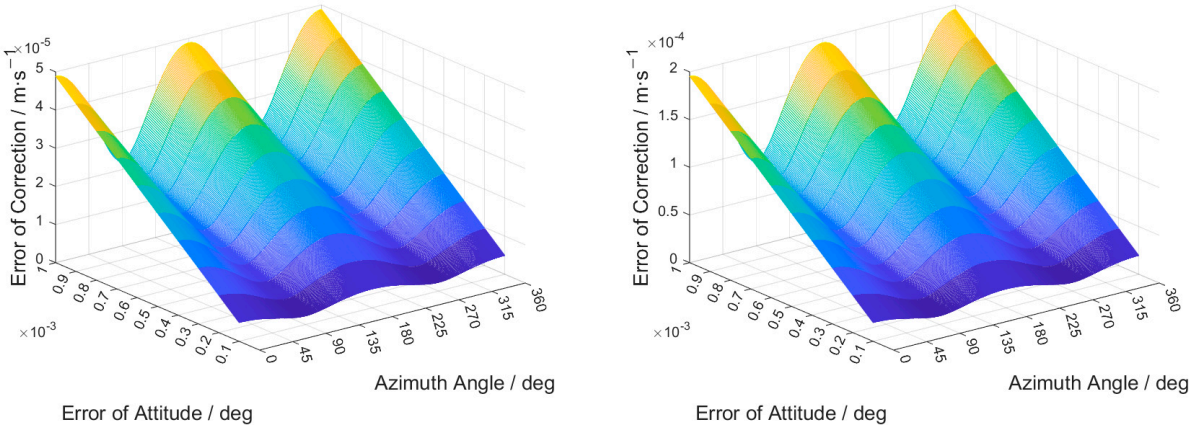

Figure 19. Total effects of attitude and height determinations on correction error. (**a**) 0.3° Beam width. (**b**) 0.6° Beam width.

Table 2. Sensitivity of velocity determination to each determination and error contribution of each determination under a 46° incidence angle.

Determinations	Sensitivity	Error Contribution
Yaw	1.61×10^{-2}	8.05×10^{-6} m·s^{-1}
Pitch	1.55×10^{-2}	7.77×10^{-6} m·s^{-1}
Roll	3.31×10^{-2}	1.61×10^{-5} m·s^{-1}
Platform Height	2.30×10^{-6}	6×10^{-8} m·s^{-1}

Compared with the required accuracy (0.1 m/s) of ocean surface currents, these values are relatively small and can be ignored. Therefore, we can conclude that under the measurement accuracy, the influence of the Doppler centroid offset on the ocean surface velocity measurement can be accurately corrected by the correction method proposed in Section 3.

5. Conclusions

For a Ka-band pencil-beam rotating Doppler scatterometer operating at a middle incidence angle, the Doppler frequency of the received signal is mainly the relative motion between ocean surface and the scatterometer. In this relative motion, the ocean surface motion is the information we need. However, the platform velocity of the spaceborne Doppler scatterometer is much higher than the ocean surface motion, so the high platform velocity accounts for the main part of the Doppler frequency. The accurate correction of the platform velocity contribution is the first and most important step for us to measure the ocean surface velocity from the received signals of a spaceborne Doppler scatterometer.

To accurately correct the high platform velocity contribution, we established a simulation model to analyze the platform velocity influence on the measurement. The model is based on the spaceborne Doppler scatterometer's observing geometry and the pulse–pair method. We simulated the measurements under spaceborne conditions and found an offset between the radial velocity measured by the pulse–pair method and the real ocean surface velocity. We found that the offset source was the offset of the actual Doppler centroid and the geometric center of the footprint. We established the correction method for this offset and factored in the antenna pattern contribution. Also, we analyzed the effects of the satellite attitude and height determinations on the correction accuracy.

Our study results confirm the importance of a high platform velocity on the ocean surface velocity measurement, which affects the accuracy of the estimation of the ocean surface motion. The offset could lead to a measurement offset of up to 0.02 m/s when the beam width was 0.3°. For the 0.6° beam width, the maximum offset was 0.07 m/s. With

the high accuracy of the current spaceborne sensors' measurement, it can be considered that this offset can be accurately eliminated. In future applications and data processing algorithms, this effect should be considered.

Past studies have proven that ocean current speed retrieval accuracy is sensitive to the accuracy of satellite attitude determination and velocity, and indicated the great importance of platform velocity elimination to ocean current retrieval. Our study complements these results, indicating that the offset of the actual Doppler centroid and the geometric center of the footprint can affect the accuracy of the ocean surface velocity measurement. To estimate the scatterometer motion's contribution to the Doppler frequency of interest, we must also measure the accurate scatterometer attitude and height parameters. Further, accurate Doppler frequency estimation requires the development of a Doppler frequency model. In parallel, the development of the related theory will also promote the development of spaceborne sensors.

Author Contributions: Conceptualization, J.Z., X.D. and D.Z.; methodology, J.Z.; software, J.Z.; validation, X.D. and D.Z.; formal analysis, J.Z.; investigation, J.Z. and D.Z.; resources, J.Z.; data curation, J.Z.; writing—original draft preparation, J.Z.; writing—review and editing, X.D.; visualization, D.Z.; supervision, X.D.; project administration, D.Z.; funding acquisition, D.Z. All authors have read and agreed to the published version of the manuscript.

Funding: This research was funded by the "Strategic Priority Research Program" of the Chinese Academy of Sciences, grant number E029122A1S.

Data Availability Statement: No new data were created or analyzed in this study. Data sharing is not applicable to this article.

Conflicts of Interest: The authors declare no conflict of interest.

References

1. Chen, R.; Flierl, G.R.; Wunsch, C. A Description of Local and Nonlocal Eddy–Mean Flow Interaction in a Global Eddy-Permitting State Estimate. *J. Phys. Oceanogr.* **2014**, *44*, 2336–2352. [CrossRef]
2. Ferrari, R.; Wunsch, C. Ocean Circulation Kinetic Energy: Reservoirs, Sources, and Sinks. *Annu. Rev. Fluid Mech.* **2009**, *41*, 253–282. [CrossRef]
3. Wang, S.D.; Shen, Y.M.; Zheng, Y.H. Two-dimensional numerical simulation for transport and fate of oil spills in seas. *Ocean. Eng.* **2005**, *32*, 1556–1571. [CrossRef]
4. Lévy, M.; Franks, P.J.S.; Smith, K.S. The role of submesoscale currents in structuring marine ecosystems. *Nat. Commun.* **2018**, *9*, 4758. [CrossRef] [PubMed]
5. Lumpkin, R.; Johnson, G.C. Global ocean surface velocities from drifters: Mean, variance, El Niño–Southern Oscillation response, and seasonal cycle. *J. Geophys. Res. Ocean.* **2013**, *118*, 2992–3006. [CrossRef]
6. Gould, J.; Sloyan, B.; Visbeck, M. Chapter 3—In Situ Ocean Observations: A Brief History, Present Status, and Future Directions. In *International Geophysics*; Siedler, G., Griffies, S.M., Gould, J., Church, J.A., Eds.; Academic Press: Cambridge, MA, USA, 2013; Volume 103, pp. 59–81.
7. Wunsch, C.; Gaposchkin, E.M. On using satellite altimetry to determine the general circulation of the oceans with application to geoid improvement. *Rev. Geophys.* **1980**, *18*, 725–745. [CrossRef]
8. Lagerloef, G.S.E.; Mitchum, G.T.; Lukas, R.B.; Niiler, P.P. Tropical Pacific near-surface currents estimated from altimeter, wind, and drifter data. *J. Geophys. Res. Ocean.* **1999**, *104*, 23313–23326. [CrossRef]
9. Ducet, N.; Le Traon, P.Y.; Reverdin, G. Global high-resolution mapping of ocean circulation from TOPEX/Poseidon and ERS-1 and -2. *J. Geophys. Res. Ocean.* **2000**, *105*, 19477–19498. [CrossRef]
10. Mouche, A.A.; Chapron, B.; Reul, N.; Collard, F. Predicted Doppler shifts induced by ocean surface wave displacements using asymptotic electromagnetic wave scattering theories. *Waves Random Complex Media* **2008**, *18*, 185–196. [CrossRef]
11. Hansen, M.W.; Collard, F.; Dagestad, K.F.; Johannessen, J.A.; Fabry, P.; Chapron, B. Retrieval of Sea Surface Range Velocities From Envisat ASAR Doppler Centroid Measurements. *IEEE Trans. Geosci. Remote Sens.* **2011**, *49*, 3582–3592. [CrossRef]
12. Goldstein, R.M.; Zebker, H.A. Interferometric radar measurement of ocean surface currents. *Nature* **1987**, *328*, 707–709. [CrossRef]
13. Romeiser, R.; Johannessen, J.; Chapron, B.; Collard, F.; Kudryavtsev, V.; Runge, H.; Suchandt, S. Direct Surface Current Field Imaging from Space by Along-Track InSAR and Conventional SAR. In *Oceanography from Space: Revisited*; Barale, V., Gower, J.F.R., Alberotanza, L., Eds.; Springer: Dordrecht, The Netherlands, 2010; pp. 73–91.
14. Chapron, B.; Collard, F.; Ardhuin, F. Direct measurements of ocean surface velocity from space: Interpretation and validation. *J. Geophys. Res. Ocean.* **2005**, *110*, C07008. [CrossRef]

15. Martin, A.C.H.; Gommenginger, C.; Marquez, J.; Doody, S.; Navarro, V.; Buck, C. Wind-wave-induced velocity in ATI SAR ocean surface currents: First experimental evidence from an airborne campaign. *J. Geophys. Res. Ocean.* **2016**, *121*, 1640–1653. [CrossRef]
16. Fois, F.; Hoogeboom, P.; Le Chevalier, F.; Stoffelen, A.; Mouche, A. DopSCAT: A mission concept for simultaneous measurements of marine winds and surface currents. *J. Geophys. Res. Ocean.* **2015**, *120*, 7857–7879. [CrossRef]
17. Rodriguez, E. On the Optimal Design of Doppler Scatterometers. *Remote Sens.* **2018**, *10*, 1765. [CrossRef]
18. Rodríguez, E.; Wineteer, A.; Perkovic-Martin, D.; Gál, T.; Stiles, B.W.; Niamsuwan, N.; Rodriguez Monje, R. Estimating Ocean Vector Winds and Currents Using a Ka-Band Pencil-Beam Doppler Scatterometer. *Remote Sens.* **2018**, *10*, 576. [CrossRef]
19. Rodríguez, E.; Wineteer, A.; Perkovic-Martin, D.; Gál, T.; Anderson, S.; Zuckerman, S.; Stear, J.; Yang, X. Ka-Band Doppler Scatterometry over a Loop Current Eddy. *Remote Sens.* **2020**, *12*, 2388. [CrossRef]
20. Yurovsky, Y.Y.; Kudryavtsev, V.N.; Grodsky, S.A.; Chapron, B. Sea Surface Ka-Band Doppler Measurements: Analysis and Model Development. *Remote Sens.* **2019**, *11*, 839. [CrossRef]
21. Abeysekera, S.S. Performance of pulse-pair method of Doppler estimation. *IEEE Trans. Aerosp. Electron. Syst.* **1998**, *34*, 520–531. [CrossRef]
22. Du, Y.; Dong, X.; Jiang, X.; Zhang, Y.; Zhu, D.; Sun, Q.; Wang, Z.; Niu, X.; Chen, W.; Zhu, C.; et al. Ocean surface current multiscale observation mission (OSCOM): Simultaneous measurement of ocean surface current, vector wind, and temperature. *Prog. Oceanogr.* **2021**, *193*, 102531. [CrossRef]
23. Weissman, D.E.; Johnson, J.W. Measurements of ocean wave spectra and modulation transfer function with the airborne two-frequency scatterometer. *J. Geophys. Res.* **1986**, *91*, 2450–2460. [CrossRef]
24. Ardhuin, F.; Aksenov, Y.; Benetazzo, A.; Bertino, L.; Brandt, P.; Caubet, E.; Chapron, B.; Collard, F.; Cravatte, S.; Delouis, J.M.; et al. Measuring currents, ice drift, and waves from space: The Sea surface KInematics Multiscale monitoring (SKIM) concept. *Ocean Sci.* **2018**, *14*, 337–354. [CrossRef]
25. Strugarek, D.; Sośnica, K.; Arnold, D.; Jäggi, A.; Zajdel, R.; Bury, G. Satellite laser ranging to GNSS-based Swarm orbits with handling of systematic errors. *GPS Solut.* **2022**, *26*, 104. [CrossRef]
26. Willis, P.; Lemoine, F.G.; Moreaux, G.; Soudarin, L.; Ferrage, P.; Ries, J.; Otten, M.; Saunier, J.; Noll, C.; Biancale, R.; et al. The International DORIS Service (IDS): Recent Developments in Preparation for ITRF2013. In *IAG 150 Years, Proceedings of the 2013 IAG Scientific Assembly, Postdam, Germany, 1–6 September 2013*; Springer: Cham, Switzerland, 2016; pp. 631–640.
27. Massmann, F.H.; Flechtner, F.; Raimondo, J.C.; Reigber, C. Impact of PRARE on ERS-2 POD. *Adv. Space Res.* **1997**, *19*, 1645–1648. [CrossRef]
28. Li, K.; Zhou, X.; Guo, N.; Zhou, S. Effect of PCV and attitude on the precise orbit determination of Jason-3 satellite. *J. Appl. Geod.* **2022**, *16*, 143–150. [CrossRef]
29. Yu, Z.; Chen, Z.; Zheng, W.J.; Zhao, R.; Xu, Z. High-precision Positioning Method for BD3 System Based on Adaptive Optimization. *J. Phys. Conf. Ser.* **2023**, *2418*, 012078. [CrossRef]
30. Bolandi, H.; Haghparast, M.; Saberi, F.F.; Vaghei, B.G.; Smailzadeh, S.M. Satellite Attitude Determination and Contol. *Meas. Control.* **2012**, *45*, 151–157. [CrossRef]
31. Bao, Q.; Lin, M.; Zhang, Y.; Dong, X.; Lang, S.; Gong, P. Ocean Surface Current Inversion Method for a Doppler Scatterometer. *IEEE Trans. Geosci. Remote Sens.* **2017**, *55*, 6505–6516. [CrossRef]
32. Miao, Y.; Dong, X.; Zhu, D. Analyzing Effects of Satellite Attitude and Speed Errors on Ocean Current Retrieval for a Doppler Scatterometer. *Prog. Electromagn. Res. M* **2021**, *106*, 139–152. [CrossRef]
33. Zhang, J.; Dong, X.; Zhu, D. Analysis of Doppler spectrum of a spaceborne Doppler scatterometer using an echoed signal simulation model. *Int. J. Remote Sens.* **2023**, *44*, 4883–4910. [CrossRef]
34. Fukao, S.; Hamazu, K. (Eds.) Radar Measurements and Scatterer Parameters. In *Radar for Meteorological and Atmospheric Observations*; Springer: Tokyo, Japan, 2014; pp. 33–73.
35. Fukao, S.; Hamazu, K. (Eds.) Principle of Doppler Velocity Measurement. In *Radar for Meteorological and Atmospheric Observations*; Springer: Tokyo, Japan, 2014; pp. 75–104.
36. Fukao, S.; Hamazu, K. (Eds.) Reception and Processing of Signals. In *Radar for Meteorological and Atmospheric Observations*; Springer: Tokyo, Japan, 2014; pp. 105–166.
37. Li, X.; Wang, C.; Qin, Z.; He, J.; Liu, F.; Sun, Q. A Velocity Dealiasing Algorithm on Frequency Diversity Pulse-Pair for Future Geostationary Spaceborne Doppler Weather Radar. *Atmosphere* **2018**, *9*, 234. [CrossRef]
38. Pazmany, A.L.; Galloway, J.C.; Mead, J.B.; Popstefanija, I.; McIntosh, R.E.; Bluestein, H.W. Polarization Diversity Pulse-Pair Technique for Millimeter-WaveDoppler Radar Measurements of Severe Storm Features. *J. Atmos. Ocean. Technol.* **1999**, *16*, 1900–1911. [CrossRef]
39. Toporkov, J.V.; Brown, G.S. Numerical simulations of scattering from time-varying, randomly rough surfaces. *IEEE Trans. Geosci. Remote Sens.* **2000**, *38*, 1616–1625. [CrossRef]
40. Walker, D. Experimentally motivated model for low grazing angle radar Doppler spectra of the sea surface. *IEEE Proc. Radar Sonar Navig.* **2000**, *147*, 114–120. [CrossRef]
41. Bird, T.S. Reflector Antennas. In *Handbook of Antenna Technologies*; Chen, Z.N., Liu, D., Nakano, H., Qing, X., Zwick, T., Eds.; Springer: Singapore, 2016; pp. 853–922.
42. Nishihama, M.; Wolfe, R.; Solomon, D. MODIS Level 1A Earth Location: Algorithm Theoretical Basis Document Version 3.0. Available online: https://modis.gsfc.nasa.gov/data/atbd/atbd_mod28_v3.pdf (accessed on 9 October 2023).

43. Sun, X.; Mao, X.; Chen, P. High-precision attitude determination using spaceborne gravity gradiometer and gyroscope. *Acta Astronaut.* **2022**, *200*, 213–225. [CrossRef]
44. Guo, J.; Zhao, Q.; Geng, T.; Su, X.; Liu, J. Precise Orbit Determination for COMPASS IGSO Satellites During Yaw Maneuvers. In *China Satellite Navigation Conference (CSNC) 2013 Proceedings*; Springer: Berlin/Heidelberg, Germany, 2013; pp. 41–53.